Journal of Archaeological Science 40 (2013) 1454–1470

Contents lists available at SciVerse ScienceDirect

Journal of Archaeological Science

journal homepage: http://www.elsevier.com/locate/jas

Integration of geophysical surveys, ground hyperspectral measurements, aerial and satellite imagery for archaeological prospection of prehistoric sites: the case study of Vésztő-Mágor Tell, Hungary

Apostolos Sarris [a], Nikos Papadopoulos [a], Athos Agapiou [b,*], Maria Cristina Salvi [a], Diofantos G. Hadjimitsis [b], William A. Parkinson [c], Richard W. Yerkes [d], Attila Gyucha [e], Paul R. Duffy [f]

[a] Laboratory of Geophysical-Satellite Remote Sensing & Archaeo-environment, Institute for Mediterranean Studies, Foundation for Research & Technology, Hellas (F.O.R.T.H.), Greece
[b] Department of Civil Engineering and Geomatics, Faculty of Engineering and Technology, Cyprus University of Technology, 2-6 Saripolou Str., Achilleos 1A, 1st Floor, 3603 Limassol, Cyprus
[c] Field Museum of Natural History, Chicago, IL, USA
[d] Ohio State University, Columbus, OH, USA
[e] Center for National Heritage Protection, Hungarian National Museum, Szeged, Hungary
[f] University of Toronto, Ontario, Canada

ARTICLE INFO

Article history:
Received 27 April 2012
Received in revised form
11 October 2012
Accepted 2 November 2012

Keywords:
Remote sensing archaeology
Geophysical surveys
Spectroradiometric measurements
Satellite and aerial images
Archaeological prospection

ABSTRACT

An integration of geophysical surveys, ground hyperspectral data, aerial photographs and high resolution satellite imagery for supporting archaeological investigations at the multi-component Vésztő-Mágor Tell, located in the southeastern Great Hungarian Plain, is presented in this study. This is one of the first times that all these techniques have been combined and evaluated for retrieving archaeological information. Geophysical explorations, specifically magnetic gradiometry and ground penetrating radar methods, have revealed shallow linear anomalies and curvilinear rings at the Tell. The use of remote sensing images has confirmed the diverse anomalies with respect to geophysics through photointerpretation, radiometric and spatial enhancements. Moreover, several indices from ground hyperspectral data also have revealed stress vegetation anomalies. These integrated results were used to map the main areas of archaeological interest at the Vésztő-Mágor Tell and plan future excavations. It was found that these multiscalar data can be used efficiently for detecting buried archaeological features.

1. Introduction

This article synthesizes the results of different remote sensing techniques that were used to examine the multi-component Tell site of Vésztő-Mágor in southeastern Europe. Remote sensing observations are well established and widely practised within archaeological research and involve a group of non-destructive methods for discovering and mapping visible and buried archaeological remains (De Laet et al., 2007; Rowlands and Sarris, 2007). Many different techniques have been used for monitoring archaeological sites within their environmental contexts. For instance, Hadjimitsis et al. (2009) have used multi-temporal satellite images and GIS spatial analysis in order to examine the urban growth in the vicinity of archaeological sites in Cyprus. The use of high spatial resolution remote sensing satellite data, has allowed Jahjah et al. (2007) to capture the integral mutations due to human interventions from 1980 to pre-post war, for the archaeological site of Babylon. The potential use of airborne lidar data for recording and monitoring erosion levels in environmentally fragile landscapes, at the Brecon Beacons National Park was recently demonstrated by Kincey and Challis (2010). Moreover, remote sensing techniques may be used for acquiring information regarding the preservation and integrity of monuments or historical buildings (Papadopoulos and Sarris, 2011; Soldovieri et al., 2008) and for risk assessment analysis (Hadjimitsis et al., 2011; Alexakis and Sarris, 2010). Even more, the manifold capabilities of such Earth Observation (EO) techniques have exhibited great potential for archaeological investigations and the technique has accounted for many important archaeological discoveries (Lasaponara and Masini, 2011).

* Corresponding author.
E-mail addresses: asaris@ret.forthnet.gr (A. Sarris), nikos@ims.forth.gr (N. Papadopoulos), athos.agapiou@cut.ac.cy (A. Agapiou), mcristinasalvi@gmail.com (M.C. Salvi), d.hadjimitsis@cut.ac.cy (D.G. Hadjimitsis), wparkinson@fieldmuseum.org (W.A. Parkinson), yerkes.1@osu.edu (R.W. Yerkes), gyuchaa@gmail.com (A. Gyucha), paulregisduffy@gmail.com (P.R. Duffy).

0305-4403/$ – see front matter © 2012 Elsevier Ltd. All rights reserved.
http://dx.doi.org/10.1016/j.jas.2012.11.001

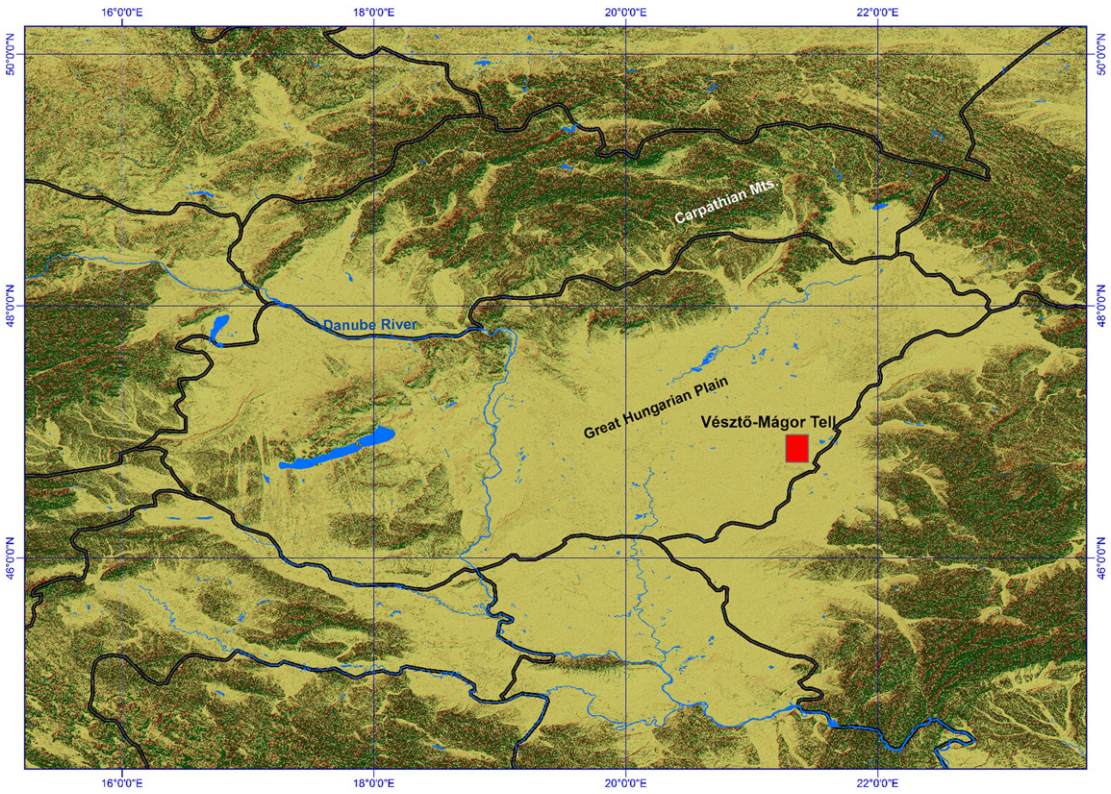

Fig. 1. The area of interest Vésztő-Mágor Tell.

The majority of remote sensing applications related to archaeological investigations are carried out based on aerial photos (oblique or vertical), satellite imagery (e.g. multispectral, hyperspectral, LiDAR) and ground geophysical surveys (Sarris, 2008). Indeed, various studies have shown that aerial and satellite imagery can be well suited for archaeological prospection (e.g. Altaweel, 2005; Masini and Lasaponara, 2007; Cavalli et al., 2007; Parcak, 2009; Traviglia, 2005; Alexakis et al., 2009, 2011). Different applications of satellite remote sensing, field studies and Geographical Information Systems (GIS) were employed on archaeological sites in India by Pappu et al. (2010). Airborne LiDAR techniques have been successfully applied by Chase et al. (2011) in investigating a Mayan archaeological site in Belize, located under a rainforest canopy. Similarly, Traviglia and Cottica (2011) argue that the implementation of aerial photographs and high resolution satellite imagery is crucial for the identification of past traces of occupation together with the ancient extent and geomorphology of the ancient islands. However as Słowik (2012) argues in his study, there are several difficulties in order to record subsurface features due to local variations of the terrain due to alluvium fills.

On a different scale, geophysical surveys also have been conducted successfully in different archaeological environments. As Batayneh (2011) mentions, geophysical methods have been used with increasing frequency in archaeology since 1946 (e.g. Jeng et al., 2003; Cardarelli and Filippo, 2009; Papadopoulos et al., 2010). The utility and limitations of geophysical surveys at alluvial plains have been demonstrated by Weston (2001). In a different environment, Drahor (2011) presented the results of geophysical investigations carried out at important archaeological sites under encroaching urbanization in the city of İzmir, Turkey.

A new ground remote sensing technique intended for archaeological investigations was recently presented by Agapiou et al. (2010, 2012) and Agapiou and Hadjimitsis (2011). In their work, ground handheld spectroradiometers were used for the detection of buried archaeological materials and features. Stressed vegetation conditions identified using crop spectral signature profiles, were successfully associated with buried remains. Although spectroradiometers were used during the past in other scientific fields such as vegetation canopy reflectance modelling, spectral mixture analysis, classification techniques or even predictive modelling (Peddle et al., 2001), very limited studies can been found in the literature regarding archaeological prospection. Ground spectroradiometers are used in the same way as airborne hyperspectral sensors (e.g. Aqdus et al., 2012). However the later need to be atmospheric and geometric corrected before any post-processing. In contrast, as Agapiou et al. (2012) argue that, *in situ* spectroradiometric data can provide more accurate results (or ground "truth") regarding the reflectance of each target since the relative distance of the instrument (spectroradiometer) and the target (crop) is relative very small (1.2 m).

In this work a major part of the Vésztő-Mágor Tell was investigated through aerial and satellite images, and ground based geophysical and spectroradiometric techniques. The aim of this study is to integrate the results of these different remote sensing approaches and to highlight their efficiency in outlining buried archaeological features.

2. Case study area

Vésztő-Mágor Tell is located on the southeastern Great Hungarian Plain (Békés County) in a meander loop of the Holt-Sebes-Körös river (Fig. 1). The Tell is composed of cultural and natural layers that cover about 4.25 ha and rise to a height of about 9 m above mean sea level (a.m.s.l; see Fig. 2, left).

The systematic archaeological investigations of the site, focusing on the monastery on top of the Tell, began in 1968 by K. Nagy and

Fig. 2. Left: Overall view at the Vésztő-Mágor Tell. Middle: View of the reconstructed remains of the monastery of the Csolt-clan. Right: Archaeological trench and *in situ* findings (through the excavation campaign in 1986) at the Tell.

continued until 1978 by I. Juhász. Excavations aiming at studying the prehistoric strata of the Tell by K. Hegedűs between 1972 and 1976, and by J. Makkay in 1986 revealed that the site was initially settled by Szakálhát Culture farmers during the late Middle Neolithic period with continuous occupation until the Late Neolithic period (c. 5000–4600 B C calibrated). On top of the Late Neolithic (Tisza Culture) levels, there is a buried humic layer signifying the abandonment of the site until the establishment of an Early Copper Age (Tiszapolgár Culture) settlement, followed by a Middle Copper Age (Bodrogkeresztúr Culture) settlement. Excavations of the Early Copper Age layer exposed more structural remains than similar sites in the area, including 20 burials of the later Tiszapolgar phase (Fig. 2, right). One more period of abandonment occurred during the end of the Middle Copper Age, and the site was reoccupied in the Early/Middle Bronze Age (Gyulavarsánd Culture) (Hegedűs, 1982; Hegedűs and Makkay, 1987; Makkay, 2004; Parkinson, 2006).

In the 11th century AD a church then a monastery of the Csolt-clan were established on the Vésztő-Mágor Tell. The monastery continued to operate until the end of the 14th century, while the two towers of the church were standing until 1798. The monastery went through different phases of construction: the early 11th century church was followed by the construction of a Romanesque style church and a rotunda church in the late 11th c. Around the church a three-naved monastery was built in the beginning of the 12th c., while reconstructions that took place at the end of the 12 c. transformed the church to a wide cathedral with two thick towers located at the west end (Juhász, 2000). In more recent periods, the Árpád period monastery, which was constructed at the southern part of the Tell, was completely destroyed by the operations that were carried out during the course of the construction of a wine cellar during the early 19th century (Hegedűs and Makkay, 1987; Juhász, 2000; Makkay, 2004.). The site became one of the Hungarian National Parks in the 1980s. Currently, in addition to the archaeological museum located within the historic wine cellar, the 1986 excavation trench can also be seen where a number of features from different periods remain *in situ* (Fig. 2 right).

3. Methodology and data collection

Diverse remote sensing techniques were applied at the site for archaeological prospection: geophysical surveys, aerial/satellite imagery and ground hyperspectral measurements. More specifically, the magnetic gradiometry techniques covered an area of 46,600 m^2 whereas the Ground Penetrating Radar (GPR) survey covered 4000 m^2 with a partial overlap of the magnetic grids towards the north central part of the site. The total area covered from the different remote sensing techniques is presented in Fig. 3.

The main aim of this study was to evaluate the potential of different ground and satellite techniques for the detection of buried layers and features. The main concept for the detection of buried features using these techniques is based on the fact that ancient remains affect topsoil and vegetation (e.g. vegetation crop marks) or they produce different magnetic and GPR signals with respect to the surrounding subsurface soil matrix. Therefore vegetation indices and spectral signature profiles obtained from multispectral satellite imagery and hyperspectral ground measurements may be used to identify areas of stressed vegetation, while advanced ground based geophysical measurements can be used to identify and map discontinuities of the soil stratigraphy or modifications of the local magnetic field caused by the presence of subsurface features. In the next section, a detailed methodology for each technique is described along with the resources and datasets used. After the final results were obtained from each method, a direct comparison and integration was made among all three methods.

3.1. Geophysical surveys

Geophysical techniques included vertical gradient magnetic techniques and GPR (Fig. 4). The total area covered by geophysical surveys is shown in Fig. 3 (left) within the grey polygon. These surveys were performed in two different phases: the first phase took place in July of 2006 focusing on the systematic wide coverage of the site through magnetic techniques, while the second phase took place in April of 2011 with the experimental employment of the GPR. The aim of both surveys was to locate subsurface features of potential archaeological significance. Processing of the geophysical data included the creation of mosaics, grid and line equalization techniques, compression of dynamic range and the application of directional filters. Processing of the GPR transects was carried out by first selecting the first peak signal for each transect and then applying AGC, Dewow and DCshift filters aiming to the enhancement of the reflected signals. Finally, horizontal depth slices at different depth levels were created by the original vertical sections assuming a velocity for the electromagnetic waves equal to 0.09 m/ns (estimated through hyperbola matching techniques). Magnetic measurements were carried out with Geoscan Research FM256 and Bartington G601 fluxgate gradiometers with a sampling of 0.5–1 m. GPR measurements employed a Sensors & Software Noggin Plus GPR unit with a 250 MHz antenna moving along parallel transects 0.5 m apart with 5 cm in-line sampling. A number of promising targets were indicated and some of them exhibited good correlation with surface monuments. The results of the geophysical survey were imported into GIS through rectification of the geophysical maps, for a further analysis of the landscape through spatial filtering techniques.

Fig. 3. Left: Entire area of the Vésztő-Mágor Tell covered from the different remote sensing techniques; Grey and blue polygons indicate the area covered from the geophysical surveys (magnetic and GPR survey respectively) while red polygon indicates the area covered from ground hyperspectral measurements. The whole area of the Tell was also been captured from satellite and aerial images (not indicated with polygon). Right: Detail map from the common area covered from all remote sensing techniques (geophysical; satellite and aerial images; ground spectroradiometric measurements) (background Google Earth©). (For interpretation of the references to colour in this figure legend, the reader is referred to the web version of this article.)

3.2. Satellite imagery

Two grayscale archive vertical aerial images provided from the Institute of Geodesy, Cartography and Remote Sensing (FÖMI) of Budapest were used in the study. The aerial images are from 1963 to 1976. Both have an approximate scale of 1:5000 (Fig. 5 left & middle). It should be mentioned that in the 1976 aerial image, open trenches of the excavations that took place in the late 60's and early 70's can be detected. Both aerial images were rectified in the WGS'84 geodetic system using ground control points. After the necessary geometric correction of the images, radiometric enhancements have been applied in order to increase the contrast and to favour the subsequent photointerpretation. Aerial photos were also subjected to spatial convolution to improve or to detect new anomalies with respect to the original images. Additional to aerial images, a high resolution multispectral GeoEye image was obtained (Fig. 5 right). The image was also georeferenced in the WGS'84 geodetic system and radiometric corrections were applied by converting the digital numbers to reflectance.

A suite of different post-processing techniques were applied to the images including spatial filters, Principal Component Analysis (PCA), Tasselled Cap algorithm (T-S), vegetation indices and histogram enhancements. All these techniques have been widely used in order to support remote sensing applications for archaeological purposes. In detail, spatial filters may be used to enhance crop marks or other edges, which are difficult to be recognized in the initial satellite image. PCA analysis, aims to create new uncorrelated data using the initial satellite imagery. In this way any statistical difference (i.e. standard deviation) of the objects is maximized. Both T-S and vegetation indices algorithms explores the key spectral characteristic of healthy vegetation (i.e. low reflectance in the red part of the spectrum and high reflectance values in the VNIR part). The majority of these indices (see Table 1) are derived from the reflectance values of the red and very near infrared bands (e.g. NDVI, SR etc). Some other indices use either the blue or the green part of spectrum along with the very near infrared (e.g. Green NDVI, ARVI etc). T-S algorithm is a linear combination of the initial bands of the images which rotate the band axes in order to enhance any

Fig. 4. The Bartington fluxgate gradiometer G601 used in the 2006 survey (left) and the NoginPlus Sensors & Software GPR unit with the 450 MHz antennas used in the 2011 survey (right) at Vésztő-Mágor Tell.

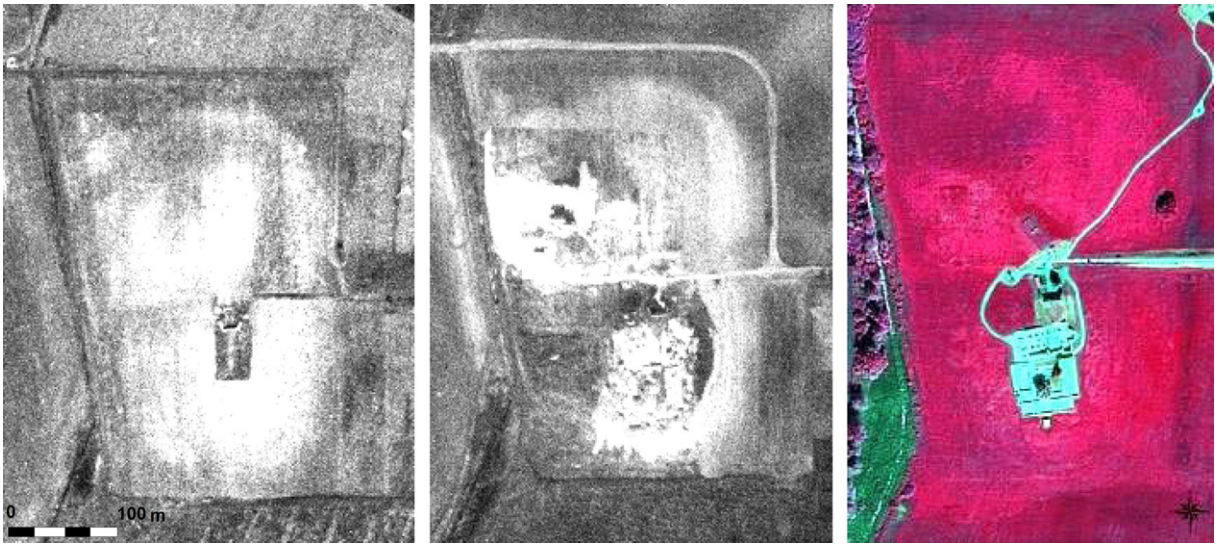

Fig. 5. Aerial image of the Vésztő-Mágor Tell acquired in 1963 (left) and 1976 (middle). Multispectral (NVIR-R-G) high resolution GeoEye image obtained in 2010 (right). The images cover an area of 300 × 350 m (WE–SN).

Table 1
Vegetation indices used for the aims of the study at the Vésztő-Mágor Tell.

Equation no	Vegetation index	Equation	Reference
Broadband			
[1]	EVI (Enhanced Vegetation Index)	$2.5\ (p_{NIR} - p_{red})/(p_{NIR} + 6\ p_{red} - 7.5\ p_{blue} + 1)$	Huete et al., 1997
[2]	Green NDVI (Green Normalized Difference Vegetation Index)	$(p_{NIR} - p_{green})/(p_{NIR} + p_{green})$	Gitelson et al., 1996
[3]	NDVI (Normalized Difference Vegetation Index)	$(p_{NIR} - p_{red})/(p_{NIR} + p_{red})$	Rouse et al., 1974
[4]	SR (Simple Ration)	p_{NIR}/p_{red}	Jordan, 1969
[5]	RDVI (Renormalized Difference Vegetation Index)	$(p_{NIR} - p_{red})/(p_{NIR} + p_{red})^{1/2}$	Roujean and Breon, 1995
[6]	PVI (Perpendicular Vegetation Index)	$(p_{NIR} - \alpha\ p_{red} - b)/(1 + \alpha^2)$ $p_{NIR,\ soil} = \alpha\ p_{red,\ soil} + b$	Richardson and Wiegand, 1977
[7]	TSAVI (Transformed Soil Adjusted Vegetation Index)	$[\alpha(p_{NIR} - \alpha\ p_{NIR} - b)]/[(p_{red} + \alpha\ p_{NIR} - \alpha b + 0.08(1 + \alpha^2))]$ $p_{NIR,\ soil} = \alpha\ p_{red,\ soil} + b$	Baret and Guyot, 1991
[8]	MSAVI (Modified Soil Adjusted Vegetation Index)	$[2\ p_{NIR} + 1 - [(2\ p_{NIR} + 1)^2 - 8(p_{NIR} - p_{red})]^{1/2}]/2$	Qi et al., 1994
[9]	GEMI (Global Environment Monitoring Index)	$n(1 - 0.25n)(p_{red} - 0.125)/(1 - p_{red})$ $n = [2(p_{NIR}^2 - p_{red}^2) + 1.5\ p_{NIR} + 0.5\ p_{red}]/(p_{NIR} + p_{red} + 0.5)$	Pinty and Verstraete, 1992
[10]	ARVI (Atmospherically Resistant Vegetation Index)	$(p_{NIR} - p_{rb})/(p_{NIR} + p_{rb})$, $p_{rb} = p_{red} - \gamma\ (p_{blue} - p_{red})$	Kaufman and Tanré, 1992
[11]	SARVI (Soil and Atmospherically Resistant Vegetation Index)	$(1 + 0.5)\ (p_{NIR} - p_{rb})/(p_{NIR} - p_{rb}\ + 0.5)$ $p_{rb} = p_{red} - \gamma\ (p_{blue} - p_{red})$	Kaufman and Tanré, 1992
[12]	DVI (Difference Vegetation Index)	$p_{NIR} - p_{red}$	Tucker, 1979
Narrowband			
[13]	CARI (Chlorophyll Absorption Ratio Index)	$p_{700}\lvert\alpha_{670} + p_{670} + b\rvert/[p_{670}(\alpha^2 + 1)^{0.5}$ $\alpha = (p_{700} - p_{550})/150$ $b = p_{550} - 550\ \alpha$	Kim et al., 1994
[14]	mNDVI (Modified Normalized Difference Vegetation Index)	$(p_{800} - p_{680})/(p_{800} + p_{680} - 2\ p_{445})$	Sims and Gamon, 2002
[15]	SR_{705} (Simple Ratio, Estimation of chlorophyll content)	p_{750}/p_{705}	Castro-Esau et al., 2006
[16]	MSAVI (Improved Soil Adjusted Vegetation Index)	$[2\ p_{800} + 1 - [(2\ p_{800} + 1)^2 - 8(p_{800} - p_{670})]^{1/2}]/2$	Qi et al., 1994
[17]	NDVI (Normalized Difference Vegetation Index)	$(p_{800} - p_{670})/(p_{800} + p_{670})$	Rouse et al., 1974
[18]	$NDVI_2$ (Normalized Difference Vegetation Index)	$(p_{750} - p_{705})/(p_{750} + p_{705})$	Gitelson and Merzlyak, 1994
[19]	SR (Simple Ratio)	p_{800}/p_{680}	Jordan, 1969
[20]	VOG (Vogelmann Indices)	p_{740}/p_{720}	Vogelmann et al., 1993
[21]	VOG_2 (Vogelmann Indices)	$(p_{734} - p_{747})/(p_{715} + p_{726})$	Zarco-Tejada et al., 2003
Leaf pigment			
[22]	ARI (Anthocyanin Reflectance Index)	$(1/p_{550}) - (1/R_{700})$	Gitelson et al., 2001
[23]	BRI (Blue Red Pigment Index)	p_{450}/p_{690}	Zarco-Tejada et al., 2005
Stress			
[24]	CI (Curvature Index)	$p_{675}.\ p_{690}/p^2{}_{683}$	Zarco-Tejada et al., 2003
[25]	NPCI (Normalized Pigment Chlorophyll index)	$(p_{680} - p_{430})/(p_{680} + p_{430})$	Peñuelas et al., 1994
Water			
[26]	fWBI (floating Water Band Index)	$p_{900}/\min\ p_{920-980}$	Peñuelas et al., 1993

p_{NIR} is the near infrared reflectance.
p_{red} is the red reflectance.
p_{green} is the green reflectance.
p_{blue} is the blue reflectance.
p_x is the reflectance at a specific wavelength.

difference occurred in vegetation. The first three new axes correspond to brightness, greenness and yellowness (soil, healthy vegetation and dry vegetation respectively). In a similar way, vegetation indices are mostly linear equations used to maximize the difference between reflectance recorded in the VNIR and the red part of the spectrum. Finally, histogram enhancement techniques are used to explore the capabilities of the image's histogram in order to improve the radiometric capability of the initial data.

3.3. Ground hyperspectral data

Ground hyperspectral data were obtained using the GER 1500 spectroradiometer that has the capability to record the reflectance to visible and near infrared spectrum, from 400 nm up to 1050 nm. GER 1500 includes 512 different narrowband channels of approximately 1.5 nm wavelength width. The Field of View (FOV) of the instrument was set up at 4° while a calibrated spectralon panel (100% Lambertian surface reflectance) was used to minimize illumination errors during the data collection (Fig. 6).

More than 1200 ground hyperspectral measurements were taken over the NW section of the Vésztő-Mágor Tell. The measurements were taken every 1 m along S–N transects which were spaced 2 m apart in W–E direction. An area of 2600 m^2 (100 m × 26 m) was surveyed with the ground spectroradiometer (see Fig. 3, red area). In each measurement, sun irradiance was measured based on the spectralon panel and afterwards the reflected radiance of the target (vegetation) was recorded. In this way the reflectance from the target could be calculated (Fig. 7). Ground spectroradiometer enabled researchers to calculate accurate reflectance values (i.e. spectral signatures), since the distance between the sensor and the target was very closed (Fig. 8).

After the necessary pre-processing, which included removal of spectral signatures and bad wavelengths, narrowband reflectance were converted to broadband reflectance using Relative Spectral Response (RSR) filters. Special attention was given to red (630–690 nm) and near infrared spectrum (760–900 nm) including the red edge (Fig. 8). Based on these two regions of the spectrum, scientists can monitor vegetation using remote sensing techniques (e.g. NDVI) and therefore any stress condition of the vegetation – due to the presence of buried archaeological features – could be easily recognized.

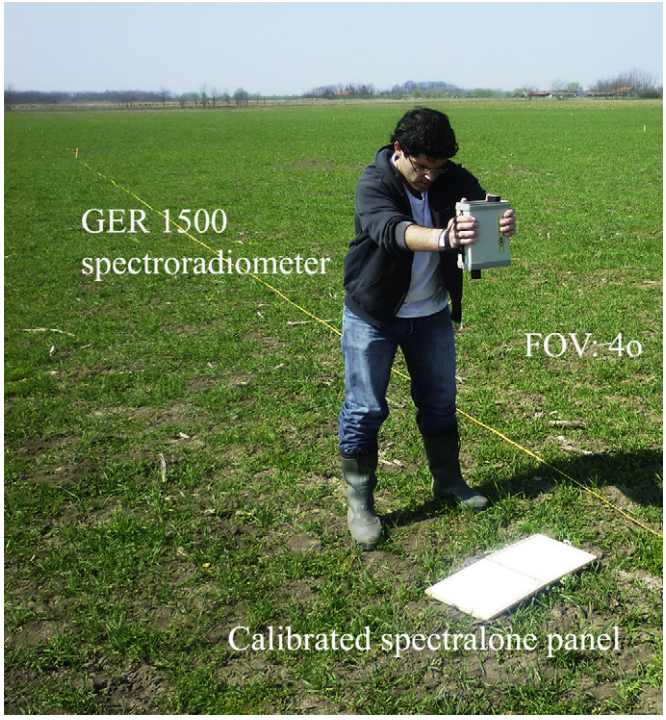

Fig. 6. The GER 1500 spectroradiometer used in order to record spectral signatures of vegetation. The calibrated spectralon panel is been used in order to minimize illumination errors during the field campaign.

After the required pre-processing of the measurements, different vegetation indices (see Table 1) were calculated in order to create the relevant thematic maps. These vegetation indices maps were produced using interpolation algorithms in a GIS environment (ArcGIS v10) for a direct comparison with the results of the aerial imagery and geophysical maps. Such indices have been reported in the literature and can be used for monitoring vegetation and characteristics of a canopy. Stagakis et al. (2010) and Agapiou et al. (2012) provide a catalogue of several indices found in the literature. Although broadband indices are widely used for archaeological prospection (e.g. NDVI, SR), there are numerous other indices that can alternatively be used for this task. Vegetation indices can be divided into five main categories according to their formulation or aim of the index: (a) broadband indices, that use broadband reflectance, (b) narrowband indices, that use narrowband reflectance (hyperspectral), (c) leaf pigment indices that examine several pigments in the leaf (e.g. Cl-a etc.), (d) stress indices which monitor stress conditions in canopy and (e) water stress indices (Stagakis et al., 2010).

4. Results

4.1. Geophysical surveys

Figs. 9 and 10 show the GPR horizontal slices with increasing depth and the magnetic results, respectively. The north section of the area was saturated with water and the GPR electromagnetic signals were completely attenuated (Sarris and Papadopoulos, 2011).

According to the magnetic data, a shallow linear anomaly (anomaly M2 at Fig. 10 right) appears to the north that has been hypothesized to belong to the north boundary of the old monastery's yard (Sarris, 2006). According to the GPR data (Fig. 9), this anomaly seems to consist of two parallel features, about 2 m apart, running in a direction W–E (feature A at Fig. 10 right). Signs of the surrounding ditches of the Tell become visible from the reflective signals of the GPR from the depth of 1.2–1.3 m and extend up to the depth of 1.7–1.8 m in a relative good correlation to the magnetic results (feature B at Fig. 10 right). Finally, as we move towards the Tell to the south, a number of intense reflectors appear especially from depths of 70–80 cm and below, but their outline is fuzzy and obscured as is the situation with the magnetic anomalies in the same region, as a result of the past excavations or other historical or modern interventions in the region of the tell (feature C at Fig. 10 right).

In addition to the basic processing techniques and the application of directional derivatives that were used as edge detection techniques, a number of high-pass filters were also applied to the original vertical magnetic gradient measurements. A 3 × 3 high-pass filter was capable of sharpening the inner details of the measurements. Other edge detection filters, such as Roberts row detector and FreiChen Column Detector filters, were applied to the data. The latter was extremely successful in enhancing a subtle anomaly towards the north-east section of the area (anomaly M4/feature D at Fig. 10 right). The particular feature has a circular shape and a diameter of 20 m (Fig. 11) and its nature is questionable, as it is not clearly related to the rest archaeological features in its vicinity.

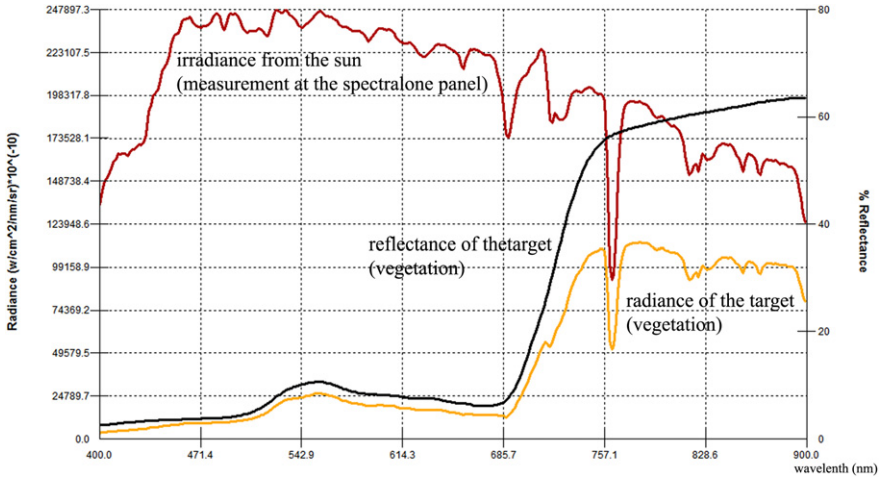

Fig. 7. Diagram showing the irradiance from the sun (measured from the spectralon panel) and the radiance at the target (vegetation). Using these two measurements the reflectance is been calculated. *X* –axis: wavelength, *Y* –axis: radiance units (left) and reflectance values (right).

The most significant archaeological features depicted by the magnetic measurements are a system of curvilinear trenches (anomalies M5, M6 at Fig. 10 right) which enclose the northern section of the Tell (Fig. 12, left) and a rectangular feature (anomalies M2, M10, M18, M17, M15 at Fig. 10 right) which encloses the whole Vésztő-Mágor Tell (Fig. 12, right). The system of curvilinear trenches is better defined at the north section, running in a direction SW–NE and then curving and changing to a NW–SE direction to the east. Thin strips of low vertical magnetic gradient values are noticed in between the two trenches. A closer look at the specific anomalies suggests that they consist of isolated smaller features that may be identified with postholes (for palisades?). Further to the north, at a distance of approximately 2–3 m there is evidence of a third trench, especially evident to the NE direction. The particular feature can be traced further to the south and it seems to turn to the SW–NE direction as it approaches the dirt road that leads to the exhibition museum.

Turning to the south, there are no clear signals that may indicate a similar pattern on the north section of the Tell. The symmetry of the curvilinear rings in the north is not as obvious as in the south.

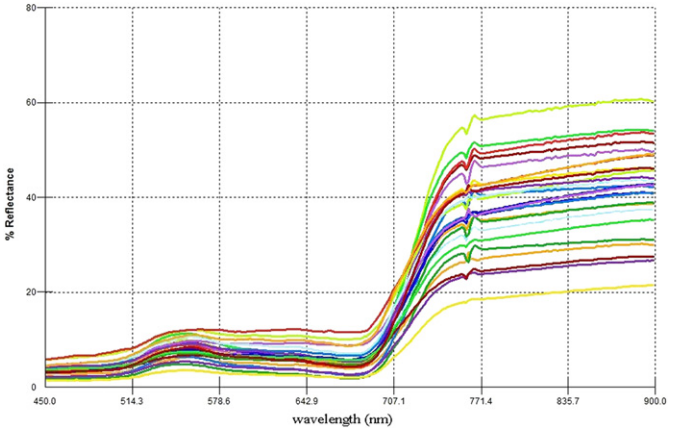

Fig. 8. Typical spectral signatures profiles derived from the GER 1500 spectroradiometer. Reflectance difference is more obvious in the VNIR part of the spectrum (760–900 nm) and the red part ("red edge", 630–700 nm). (For interpretation of the references to colour in this figure legend, the reader is referred to the web version of this article.)

The whole image of the southern side of the Tell becomes even more complicated due to the presence of the strongly magnetic segments. Linear anomalies constitute a well defined rectangular feature of approximately 135 × 260 m around the Tell. The feature is clearly defined in the SW, S and E and it is less defined in the north (Fig. 12, right). Its traces are completely lost to the NE and west side of the map. The particular feature seems to have no relationship to the curvilinear anomalies (trenches) and it probably signifies the property boundaries during the latest phases of the monastery of the Csolt-clan. These boundaries, probably walls, produced a high vertical magnetic gradient anomaly similar to the curvilinear trenches to the north. However, the width of the anomaly is less than 1.5 m compared to the width of the trenches, which varies between 3 and 4.5 m. Furthermore, the wall boundaries are laid around the Vésztő-Mágor Tell, located at the lower elevations (85.3–86 m relative altitude), whereas the north system of trenches is located at higher altitudes (86.5–88 m relative altitude). The latter elevation range is different from the elevation of the south curvilinear anomaly, which is located on the flat area extending even beyond the walls that confined the monastery grounds (Sarris, 2006).

4.2. Satellite and aerial imagery

Archive aerial photos were filtered to enhance or discover new anomalies with respect to the original images. Spatial filtering (3 × 3 edge detection filters) of an aerial image of 1963 clearly shows a path going to the north and then running to the west, nowadays invisible (Fig. 13a). This anomaly seems to be relevant and important, even if not clearly delineated, is a curved line, of 2 m width extending over the north and NE section of the original image (Fig. 13b).

Regarding the aerial image taken in 1976, spatial filters clearly show a wealth of details among which is a path or wall going to the north and then running to the west, nowadays invisible. A series of trenches are open to the west. In the central north part of the image there are features that could suggest the activity of the previous years of excavation. To the south, the excavation probably shows the scheme of the church and a series of rooms that belonged to the monastery (Fig. 13c, d).

Further to the aerial image, a GeoEye high resolution satellite image was used in the study. After the geometric and radiometric correction of the image different post-processing techniques were

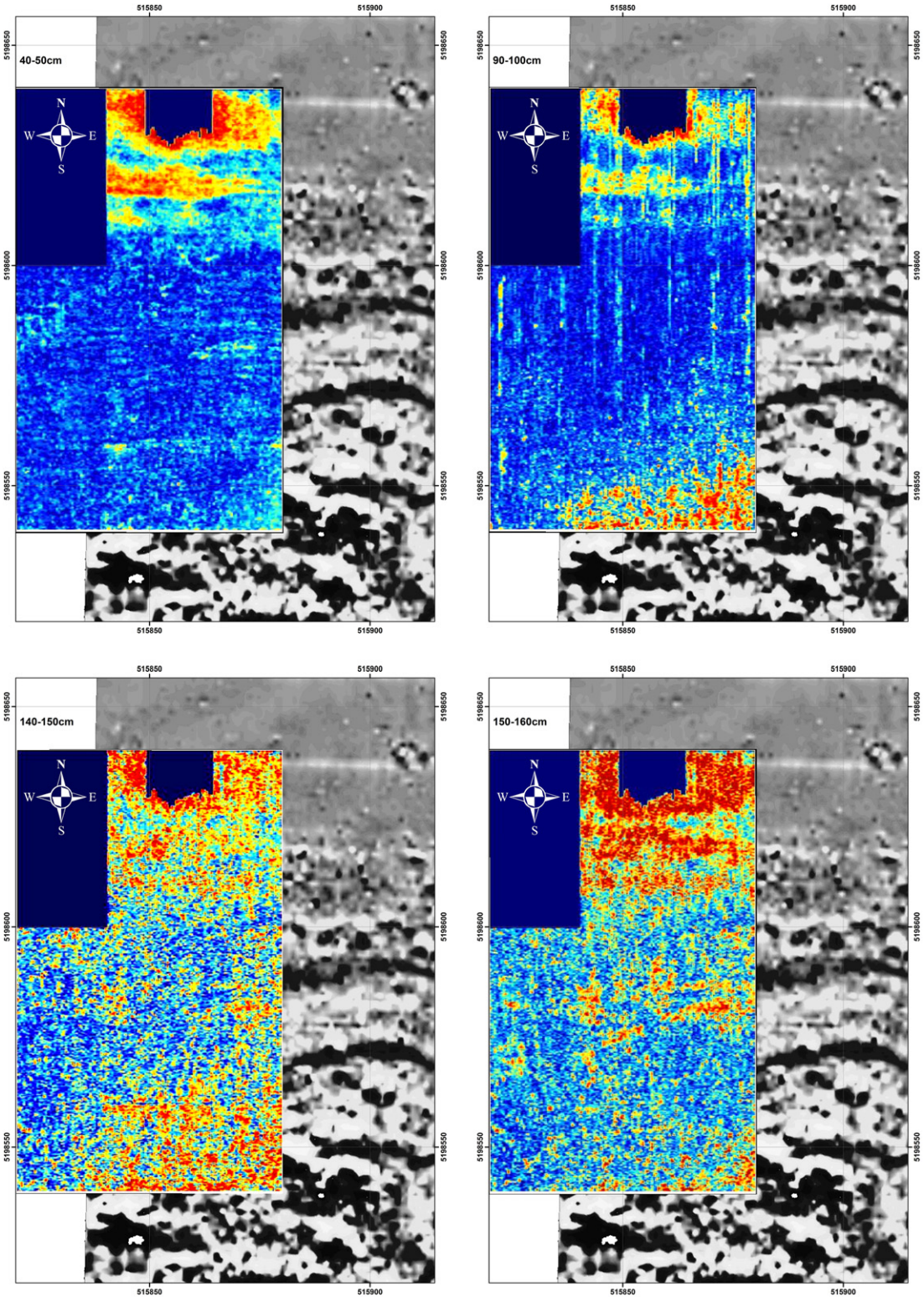

Fig. 9. Ground penetrating radar results at the Vésztő-Mágor Tell. Slices at 40–50 cm depth (top left), 90–100 cm depth (top right), 140–150 cm depth (bottom left) and 150–160 cm depth (bottom right) are shown superimposed on top of the results of the magnetic survey (see Fig. 10). The GPR slices cover an area of 60 × 100 m (WE–NS). The correspondence of the GPR grids to the magnetic grids is shown in Fig. 3.

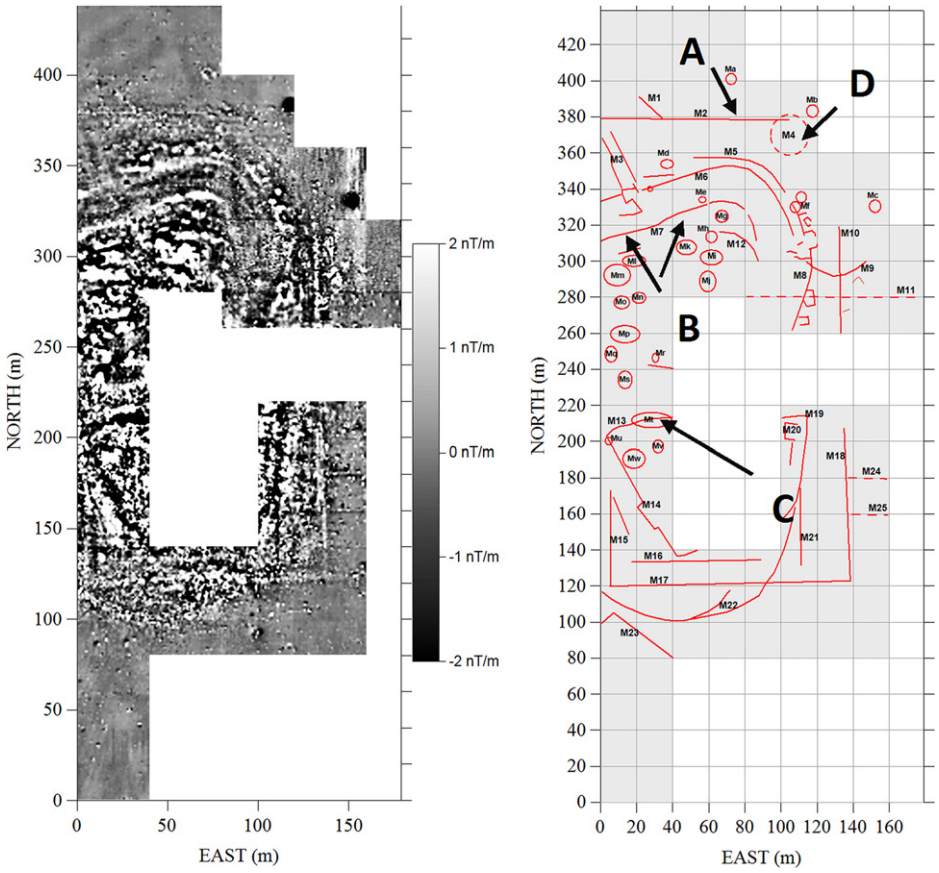

Fig. 10. The result of the compression of the dynamic range of the magnetic gradiometry measurements. The image enhances even the subtle magnetic signals and makes easier the identification of magnetic features (left). Diagrammatic interpretation of the vertical magnetic gradient data and coding of the most significant anomalies (right).

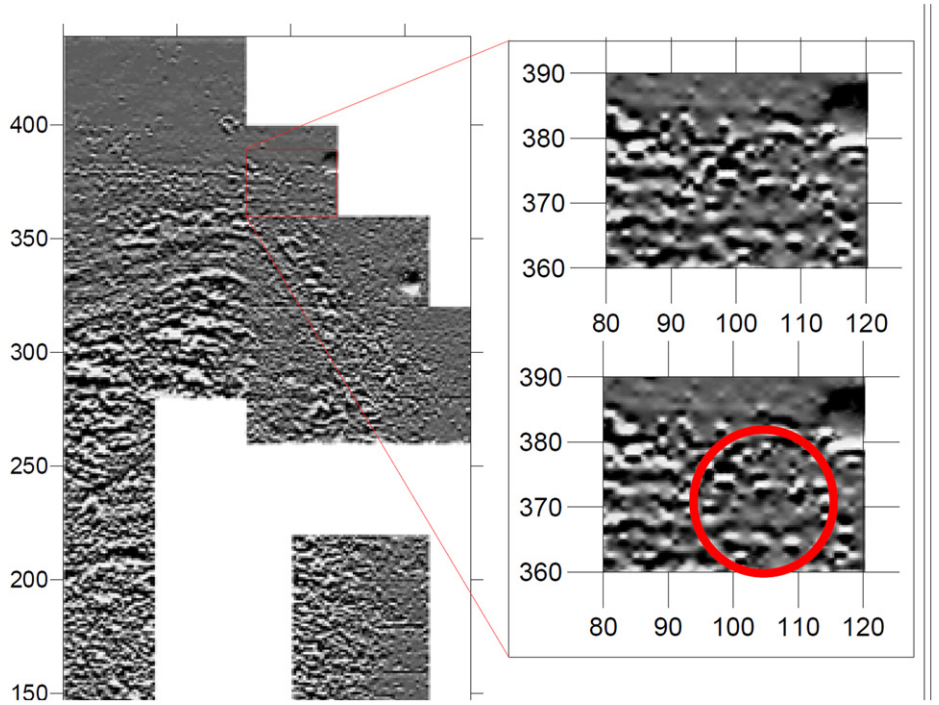

Fig. 11. Application of high-pass and edge detection filters to the vertical magnetic gradient measurements from the Vésztő-Mágor site. Magnification of the area at the north indicating a circular structure.

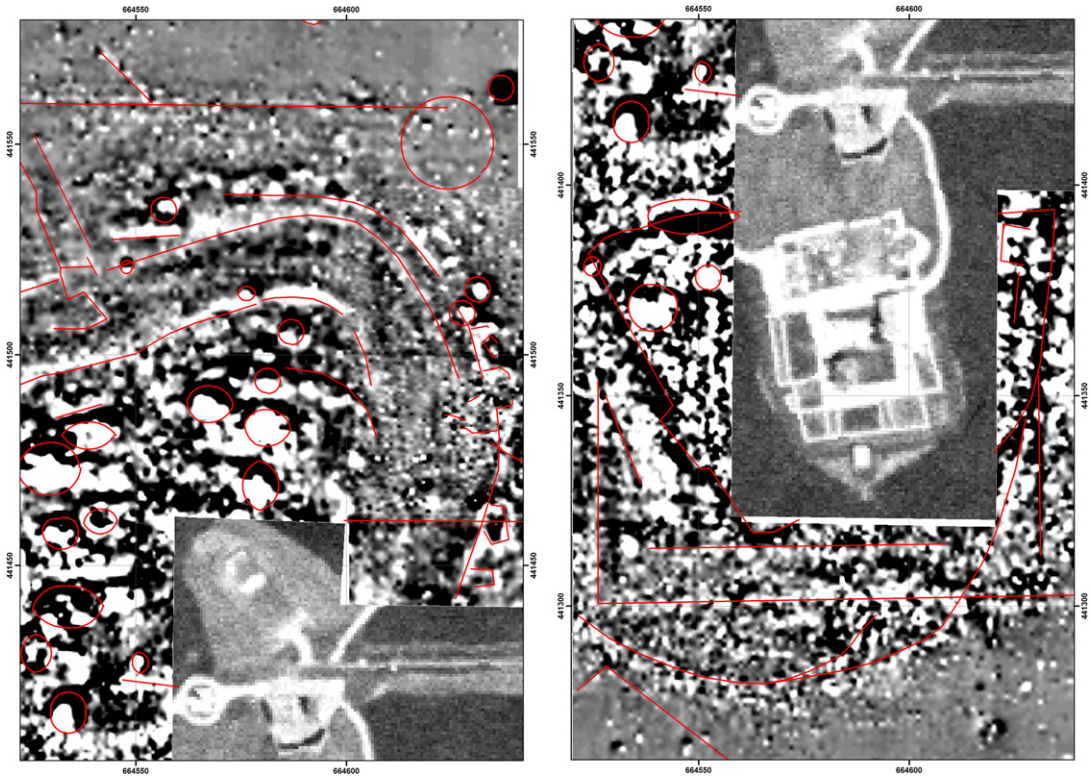

Fig. 12. Details from the north section of the surveyed region. A system of trenches is clearly identified from the magnetic survey (left). The rectangular feature which encloses the whole Vésztő-Mágor Tell (right).

applied, including convolution filters in an attempt to enhance possible anomalies on the Tell (Fig. 14, left). The filters were able to detect the boundaries of the monastery. The rest of the anomalies are not all easily distinguishable. The most evident feature is a path or wall going to the north and then running to the west, nowadays invisible. Moreover traces of the past archaeological trenches are visible towards the west central part of the image. Traces of the Tell's surrounding trenches are also visible to the south and the north of the Tell. Fig. 14 (right) highlights all the interpretation results of the satellite image.

Moreover, broadband vegetation indices have been applied to the GeoEye image. All indices have been enhanced by applying a Gaussian contrast that helped to distinguish the main features of the site, namely the old trenches and the supposed ditches. In general, the DVI index resulted superior results among the others showing in the enhanced image, a clear feature that could reveal the ditches of the ancient Tell, less, in some other Indices as the NDVI and SR (Fig. 15a–c).

Finally, PCA and T-S analysis was performed to the GeoEye image. The PCA allowed the creation of new synthetic bands with no correlated variables, and proved to be very useful in distinguishing anomalies on the tell (such as anomalies M2, M9, M18 M17, M5, a.o) (Fig. 15d). The T-S transformation, showing the Brightness, the Greenness and the Yellowness in the new generated band, did not reveal anomalies even after subsequent contrast enhancements (Fig. 15e).

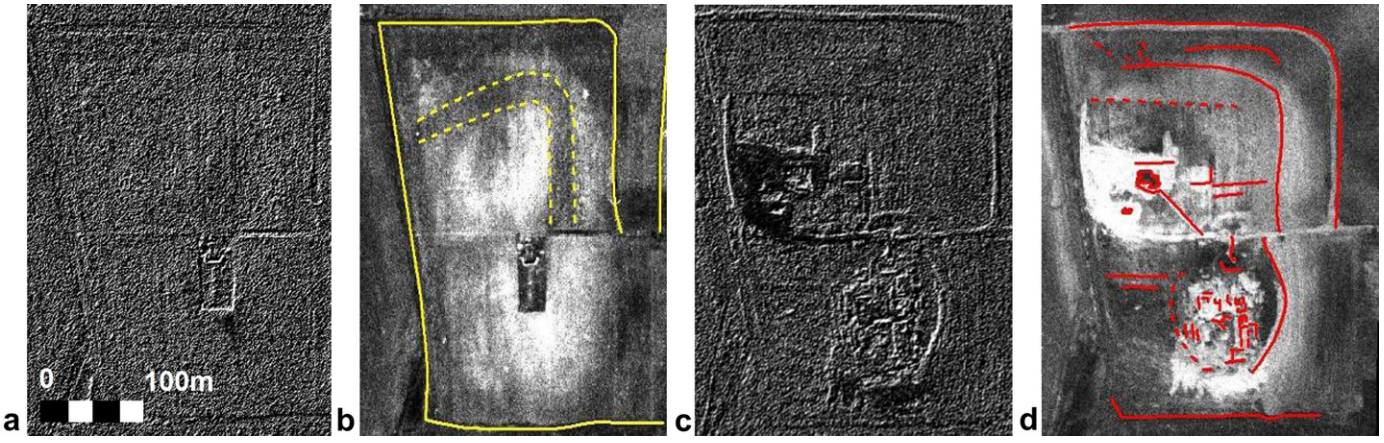

Fig. 13. Edge detection (a, c) and photointerpretation results (b, d) at aerial images taken in 1963 and 1976 respectively. The images cover an area of 300 × 350 m (WE–SN).

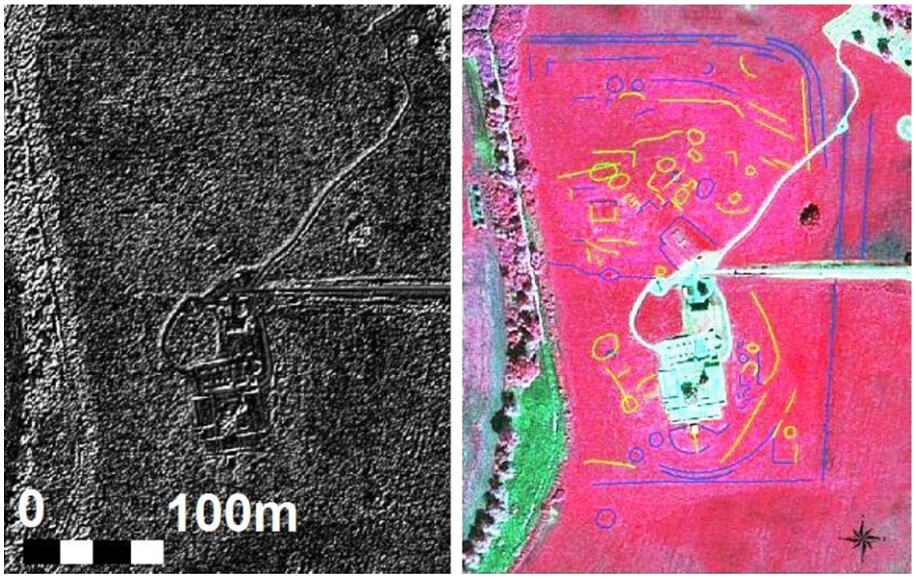

Fig. 14. Convolution filters (3 × 3 edge detection) applied in the GeoEye satellite image (left) and evidences by photointerpretation reclassified (Blue, high visibility; Yellow, medium visibility; Green, low visibility) (right). The images cover an area of 300 × 350 m (WE–SN). (For interpretation of the references to colour in this figure legend, the reader is referred to the web version of this article.)

4.3. Ground hyperspectral data

Regarding the ground spectroradiometric data, several vegetation indices were developed for the same area covered by the *in situ* measurements (see red polygon in Fig. 3) As indicated in Fig. 16 a linear (?) anomaly was detected at around 80 m (W–E orientation) for several indices. This anomaly was found not only to broadband or narrowband vegetation indices but also to other specific developed indices (e.g. fWBI for water stress detection). Indeed as it is shown in Fig. 16, the linear anomaly is recorded in the majority of the proposed by the literature indices, while some other linear anomalies can also be found (e.g. horizontal anomaly at around 40–50 m).

Statistical analysis was also applied based on the previous results. Correlation coefficient (R^2) and Principal Component Analysis (PCA) were performed in order to evaluate the different correlations between all indices of Table 1 and also to reduce the data amount without losing any significant vegetation anomaly. As shown in Fig. 17 many indices have high correlation (R^2>85%), which indicates that these indices are sensitive to common vegetation characteristics (e.g. broadband indices). On the other hand, there are several other indices with low correlation, and therefore some of them may be also used for archaeological prospection (further to broadband indices) resulting on complementary information to the above.

From PCA analysis, it was found that the first three components could explain more than 88% of the total variance of the data. The results for the first 3 components PCA1 – PCA3 are presented in Fig. 18.

A direct comparison between similar broadband and narrowband vegetation indices was also attempted. As it is shown in Fig. 19 the NDVI indices (see Equation (3), (17), (18) in Table 1) have similar results (broadband and narrowband) and in all cases linear anomalies at around 30–40 m and 80 m were recorded. Due to the numerous measurements taken in the area a compression of data was attempted in order to minimize random error. This was performed by up-scaling the resolution of data. As it was found (Fig. 20) random error was minimized and stress vegetated areas were visible in a 5 m resolution, while down-scaling of data (<1 m) did not provide any further details. Based on the results of Fig. 19, it is clear that further indices could be used in order to identify buried archaeological features. Indeed in the literature only few indices are

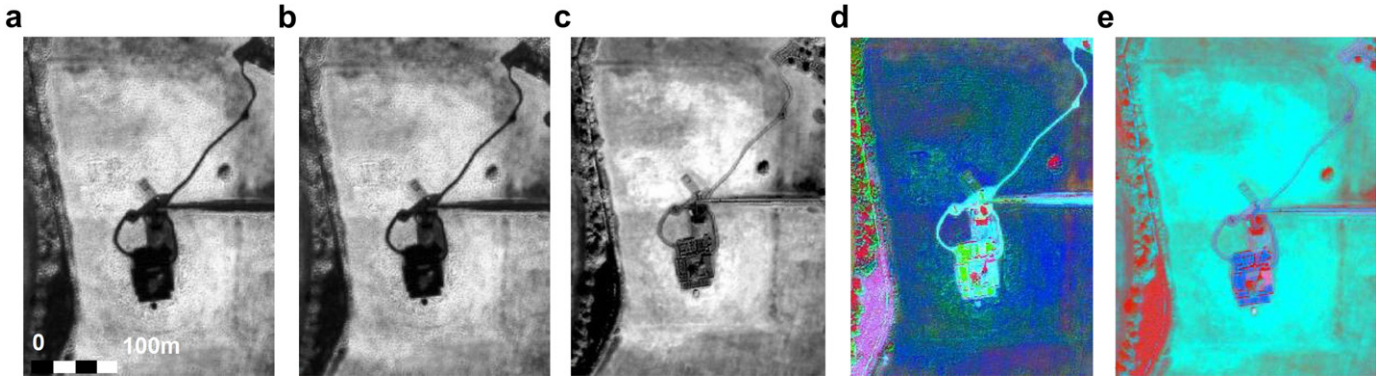

Fig. 15. Vegetation indices results: (a) SR index, (b) NDVI, (c) DVI, (d) Principal components (FCC 123) analysis and (e) Tasselled cap (FCC 321) results. The images cover an area of 300 × 350 m (WE–SN).

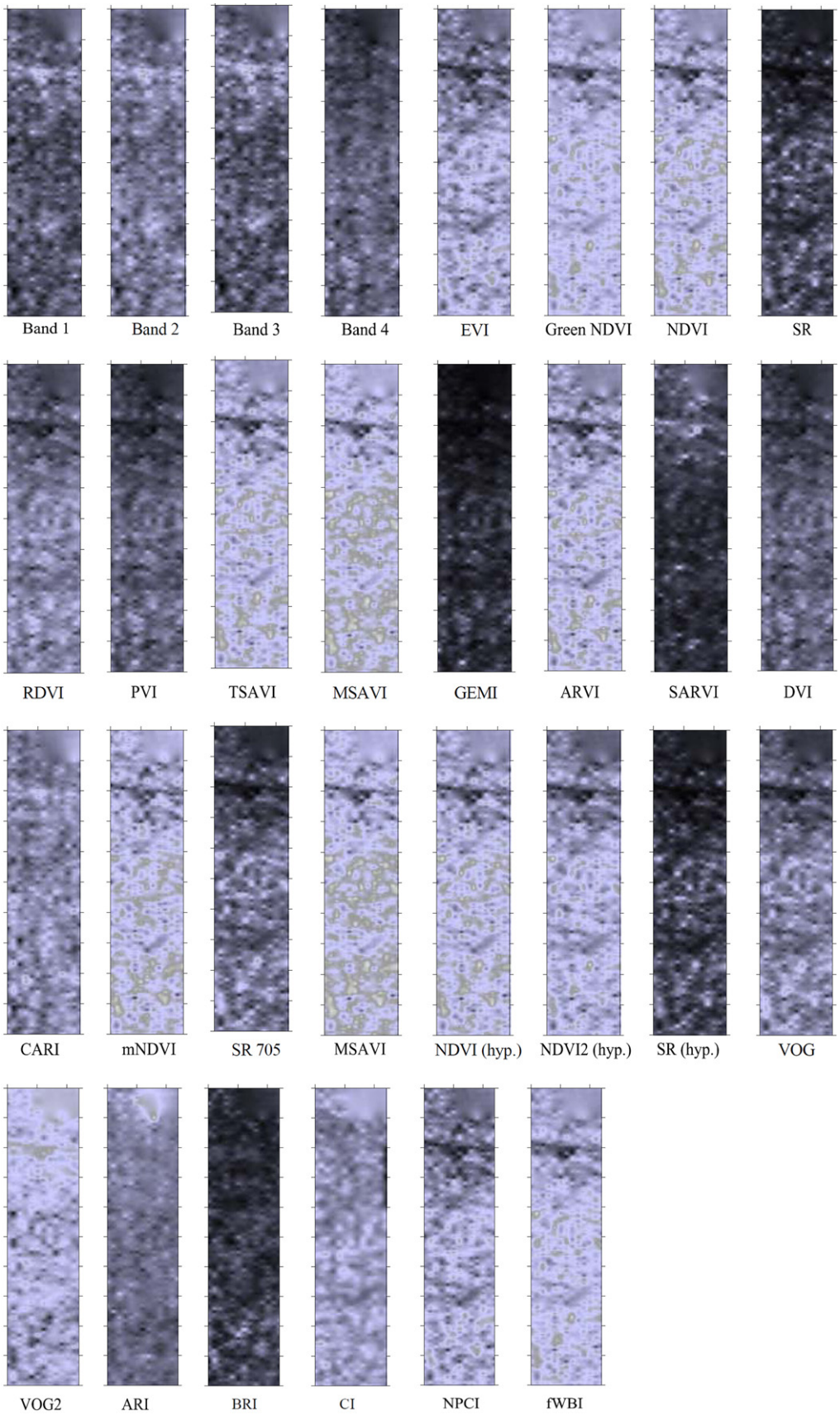

Fig. 16. Band reflectance and vegetation indices results for the area (26 × 100 m) surveyed with ground spectroradiometers. Low values of reflectance (%)/vegetation index (dimensionless) are shown with black while white colour indicates high values reflectance/vegetation index.

	EVI	Green_NDVI	NDVI	SR	RDVI	PVI	TSAVI	MSAVI	GEMI	ARVI	SARVI	DVI	CARI	mNDVI	SR705	mNDVI2	MSAVI	NDVI	NDVI2	OSAVI	RDVI	SR	VOG	VOG2	ARI	BRI	CRI	CI	NPCI	fWBI
EVI	1.00	.92	.97	.90	.85	.75	.97	.96	.72	.98	-.72	.72	-.15	.98	.92	.95	.96	.97	.95	.97	.86	.89	.89	-.71	-.57	.67	.68	.06	-.84	.87
Green_NDVI	.92	1.00	.98	.88	.85	.74	.97	.97	.71	.96	-.74	.71	-.25	.91	.94	.96	.96	.96	.98	.96	.85	.86	.93	-.74	-.38	.44	.70	.06	-.61	.80
NDVI	.97	.98	1.00	.89	.87	.76	1.00	1.00	.72	1.00	-.77	.73	-.17	.97	.93	.96	.99	1.00	.98	1.00	.88	.88	.91	-.72	-.48	.53	.70	.07	-.71	.84
SR	.90	.88	.89	1.00	.81	.73	.88	.85	.78	.90	-.59	.70	-.15	.83	.96	.89	.85	.88	.91	.88	.81	.99	.91	-.70	-.54	.60	.73	.06	-.79	.81
RDVI	.85	.85	.87	.81	1.00	.98	.87	.87	.93	.87	-.86	.97	.26	.83	.84	.85	.87	.87	.87	.88	1.00	.81	.81	-.63	-.67	.42	.46	.06	-.58	.81
PVI	.75	.74	.76	.73	.98	1.00	.76	.75	.97	.76	-.82	1.00	.41	.71	.75	.74	.75	.76	.76	.76	.98	.73	.72	-.55	-.68	.36	.34	.06	-.50	.74
TSAVI	.97	.97	1.00	.88	.87	.76	1.00	1.00	.72	1.00	-.77	.73	-.17	.97	.93	.96	1.00	1.00	.98	1.00	.88	.88	.90	-.72	-.47	.53	.69	.07	-.71	.84
MSAVI	.96	.97	1.00	.85	.87	.75	1.00	1.00	.70	.99	-.79	.72	-.17	.97	.90	.96	1.00	.99	.97	.99	.87	.84	.89	-.70	-.46	.50	.67	.07	-.68	.83
GEMI	.72	.71	.72	.78	.93	.97	.72	.70	1.00	.72	-.70	.96	.35	.66	.77	.71	.69	.72	.73	.72	.93	.78	.72	-.55	-.65	.41	.37	.06	-.55	.71
ARVI	.98	.96	1.00	.90	.87	.76	1.00	.99	.72	1.00	-.75	.73	-.17	.98	.94	.97	.99	1.00	.98	1.00	.87	.89	.91	-.72	-.51	.58	.70	.07	-.76	.85
SARVI	-.72	-.74	-.77	-.59	-.86	-.82	-.77	-.79	-.70	-.75	1.00	-.82	-.27	-.73	-.66	-.75	-.79	-.76	-.75	-.77	-.86	-.58	-.65	.48	.60	-.29	-.31	-.04	.39	-.69
DVI	.72	.71	.73	.70	.97	1.00	.73	.72	.96	.73	-.82	1.00	.45	.68	.72	.71	.72	.73	.73	.73	.97	.70	.69	-.52	-.69	.34	.30	.06	-.47	.72
CARI	-.15	-.25	-.17	-.15	.26	.41	-.17	-.17	.35	-.17	-.27	.45	1.00	-.16	-.23	-.25	-.15	-.16	-.23	-.15	.27	-.12	-.27	.28	-.41	-.16	-.42	.02	.13	-.01
mNDVI	.98	.91	.97	.83	.83	.71	.97	.97	.66	.98	-.73	.68	-.16	1.00	.87	.92	.98	.98	.93	.98	.84	.84	.84	-.66	-.49	.62	.65	.08	-.80	.83
SR705	.92	.94	.93	.96	.84	.75	.93	.90	.77	.94	-.66	.72	-.23	.87	1.00	.96	.89	.92	.97	.92	.84	.95	.97	-.78	-.53	.59	.73	.06	-.74	.84
mNDVI2	.95	.96	.96	.89	.85	.74	.96	.96	.71	.97	-.75	.71	-.25	.92	.96	1.00	.95	.95	1.00	.95	.85	.87	.96	-.78	-.52	.58	.68	.05	-.70	.85
MSAVI	.96	.96	.99	.85	.87	.75	1.00	1.00	.69	.99	-.79	.72	-.15	.98	.89	.95	1.00	1.00	.96	1.00	.87	.84	.87	-.69	-.46	.51	.66	.07	-.70	.83
NDVI	.97	.96	1.00	.88	.87	.76	1.00	.99	.72	1.00	-.76	.73	-.16	.98	.92	.95	1.00	1.00	.97	1.00	.88	.88	.89	-.70	-.48	.54	.69	.07	-.73	.84
NDVI2	.95	.98	.98	.91	.87	.76	.98	.97	.73	.98	-.75	.73	-.23	.93	.97	1.00	.96	.97	1.00	.97	.87	.89	.96	-.78	-.51	.55	.70	.06	-.70	.85
OSAVI	.97	.96	1.00	.88	.88	.76	1.00	.99	.72	1.00	-.77	.73	-.15	.98	.92	.95	1.00	1.00	.97	1.00	.88	.88	.89	-.71	-.49	.54	.69	.07	-.73	.84
RDVI	.86	.85	.88	.81	1.00	.98	.88	.87	.93	.87	-.86	.97	.27	.84	.84	.85	.87	.88	.87	.88	1.00	.81	.80	-.62	-.67	.44	.46	.07	-.60	.82
SR	.89	.86	.88	.99	.81	.73	.88	.84	.78	.89	-.58	.70	-.12	.84	.95	.87	.84	.88	.89	.88	.81	1.00	.89	-.67	-.55	.61	.73	.07	-.80	.82
VOG	.89	.93	.91	.91	.81	.72	.90	.89	.72	.91	-.65	.69	-.27	.84	.97	.96	.87	.89	.96	.89	.80	.89	1.00	-.79	-.49	.55	.69	.05	-.67	.81
VOG2	-.71	-.74	-.72	-.70	-.63	-.55	-.72	-.70	-.55	-.72	.48	-.52	.28	-.66	-.78	-.78	-.69	-.70	-.78	-.71	-.62	-.67	-.79	1.00	.37	-.43	-.60	-.04	.52	-.63
ARI	-.57	-.38	-.48	-.54	-.67	-.68	-.47	-.46	-.65	-.51	.60	-.69	-.41	-.49	-.53	-.52	-.46	-.48	-.51	-.49	-.67	-.55	-.49	.37	1.00	-.55	-.20	-.03	.57	-.60
BRI	.67	.44	.53	.60	.42	.36	.53	.50	.41	.58	-.29	.34	-.16	.62	.59	.58	.51	.54	.55	.54	.44	.61	.55	-.43	-.55	1.00	.41	.02	-.86	.58
CRI	.68	.70	.70	.73	.46	.34	.69	.67	.37	.70	-.31	.30	-.42	.65	.73	.68	.66	.69	.70	.69	.46	.73	.69	-.60	-.20	.41	1.00	.07	-.57	.54
CI	.06	.06	.07	.06	.06	.06	.07	.07	.06	.07	-.04	.06	.02	.08	.06	.05	.07	.07	.06	.07	.07	.07	.05	-.04	-.03	.02	.07	1.00	-.07	.04
NPCI	-.84	-.61	-.71	-.79	-.58	-.50	-.71	-.68	-.55	-.76	.39	-.47	.13	-.80	-.74	-.70	-.70	-.73	-.70	-.73	-.60	-.80	-.67	.52	.57	-.86	-.57	-.07	1.00	-.72
fWBI	.87	.80	.84	.81	.81	.74	.84	.83	.71	.85	-.69	.72	-.01	.83	.84	.85	.83	.84	.85	.84	.82	.82	.81	-.63	-.60	.58	.54	.04	-.72	1.00

Fig. 17. Correlation coefficients among all indices of Table 1. High correlation (R^2>85%) is marked with grey.

applied (e.g. NDVI) for supporting archaeological research. Fig. 19, demonstrates that both broadband and narrowband vegetation indices can be used in order to enhance crop marks. Based on the equation of each index some indices may be better distinguished buried archaeological relics.

5. Discussion

The use of remote sensing images, both aerial and satellite, and traditional photointerpretation confirmed the identification of features in close correlation to the rest of geophysical techniques.

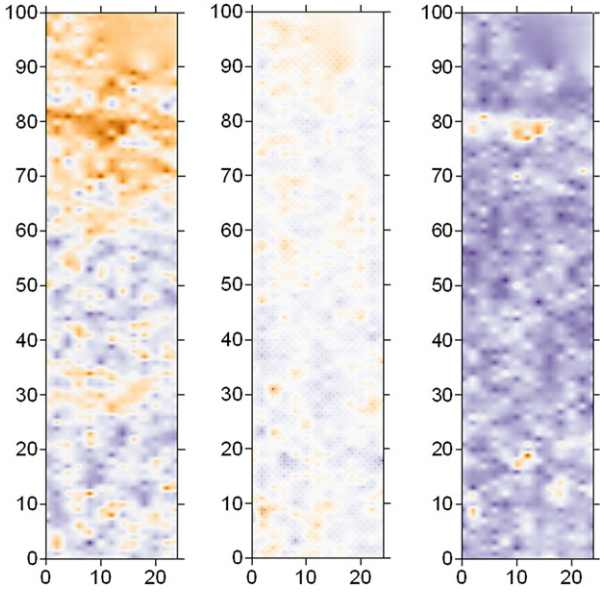

Fig. 18. PCA 1-3 (from left to right) based on all indices of Table 1.

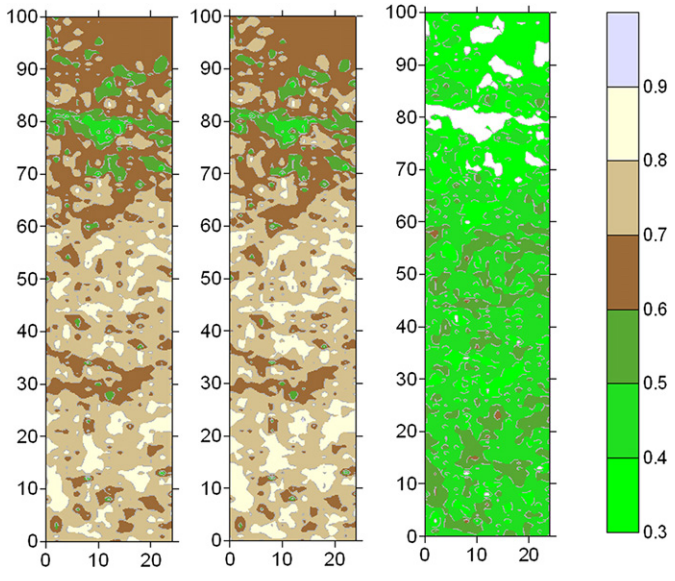

Fig. 19. Broadband NDVI result (left) and narrowband NDVI and NDVI2 results (middle and right respectively) as derived from the spectroradiometric data.

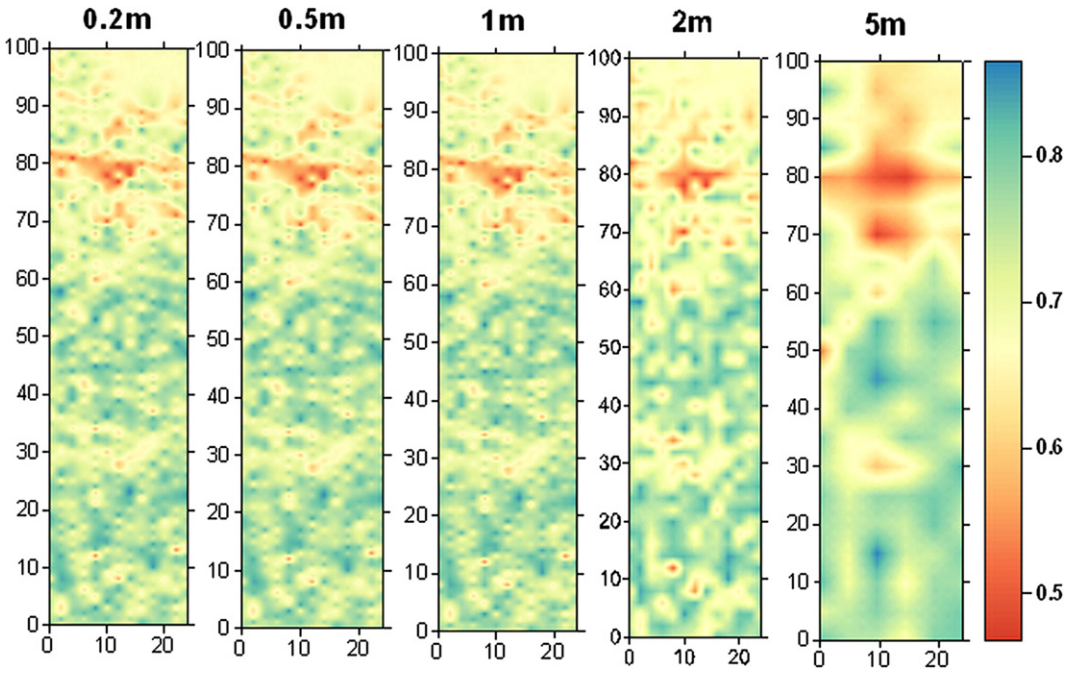

Fig. 20. Up-scaling (2 m and 5 m, right) and down-scaling (0.2 m and 0.5 m, left) results based on the original (1 m, centre) interval measurements. As it is shown, even the 5 m grid resolution map was able to detect stress vegetated areas.

Multi-temporal images revealed features that can differentiate with respect to the time capture of the images. The radiometric and spectral techniques allowed the enhancement of the anomalies present in the area.

It is very important to highlight the fact that both ground spectroradiometric and geophysical measurements were obtained in the same date. In this way any climatic or other environmental factors which could affect the measurements was minimized. The overpass of the high resolution satellite image was made only a few days later from these field campaigns. The common area under investigation (see red polygon in Fig. 3) is a fine example in order to compare these different remote sensing techniques. As it was shown from the previous section, each method could detect some archaeological features. Common features detected from these techniques allowed researchers to determine "possible archaeological sites" with great confidence. In contrast, features not revealed in all of these methods demonstrated in a clear way that each method has specific capabilities. For instance ground spectroradiometric measurements could not identify any human traces beyond 1.3 m depth as the geophysical methods did.

The comparison of new techniques with geophysical data appears to be very promising and as it has been previously suggested by Kvamme (2006) and Ernenwein (2009) their fusion may be used in the future for maximizing the information content of the subsurface of the archaeological sites. In order to give a sense of how this fusion may be applied, the authors have tried a number of algorithms (Principal Component, Multiplicative Brovery etc) for fusing together the geophysical, satellite and aerial images (Fig. 21). Still, more work in this domain has to be carried out in order to evaluate the significance of this approach and the ways of interpretation of multi- or hyper-dimensional remote sensing data.

6. Conclusions

This article presents the results of a manifold remote sensing approach (Sarris, 2012) for the Vésztő-Mágor Tell, located in the southeastern part of the Great Hungarian plain. Different remote sensing techniques were evaluated in order to enhance the final interpretation results.

Based on the remote sensing results it seems that the Vésztő-Mágor Tell consists of three curvilinear rings that outline the north section of the site. The particular features that are most probably related to foundation trenches are not circular, but curvilinear in shape. In between the trenches, traces of palisades also may be suggested by the magnetic data. A possible entrance to the settlement is located at the NW section of the area. The traces of the trenches fade away towards the east and south slopes of the Mágor Tell. A subtle curvilinear (almost circular) anomaly also is evident to the south. However, it is not possible to conclude whether the specific anomaly is part of the same system of the trenches to the north.

Furthermore, the structural details of the Tell also are difficult to identify, mainly due to the multiple occupation layers, and the disturbance of the stratigraphy by the past excavations and the historical constructions. Most of the interior anomalies which are located on the upper slopes of the Tell are of fuzzy nature and do not show any rectangular features, although some of them may indicate residues of past cultural activities. A few more linear or slightly curvilinear segments are present at the south side of the Tell, running along the same elevation contour of 87.5–88 m. If the particular anomalies belong to the same feature, they could be identified as the inner boundaries of the monastery facilities (monastery yard?). On the lower slopes, a group of N–S and E–W anomalies define a rectangular feature of dimensions 135 × 260 m, which can be correlated with the existence of a wall structure outlining the boundaries of the monastery grounds. A few more anomalies can be suggested by the magnetic data and they are probably related to a more recent utilization of the Vésztő-Mágor Tell site. In general, the most of the geophysical anomalies such as the boundaries of the historical monastery yard, the Tell ditches and the past excavation trenches were all confirmed through the processing of the

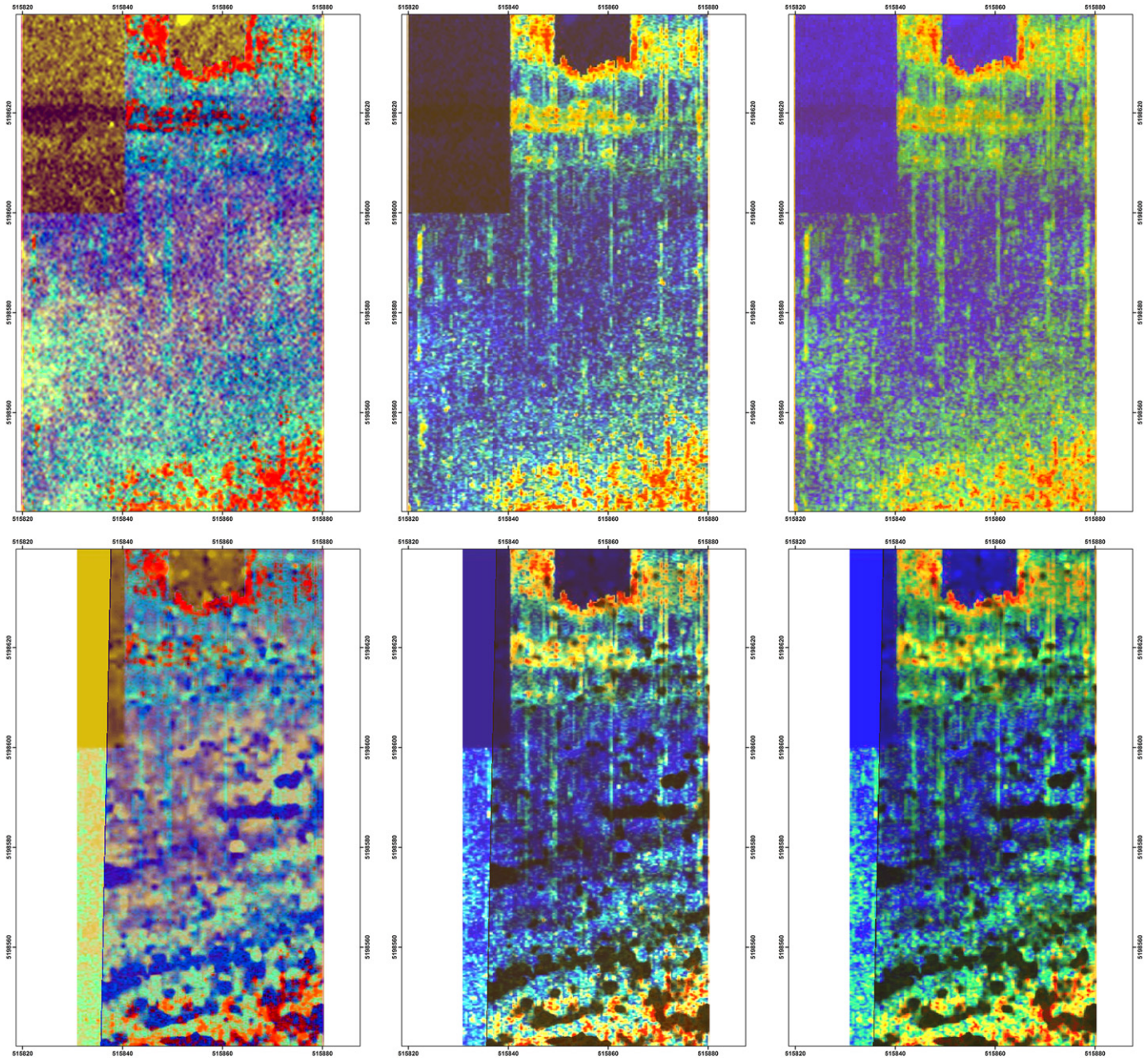

Fig. 21. Fusion between magnetic and GPR depth slices (0.90 cm and 100 cm) (above) and between the aerial image of 1963 and the GPR depth slices (0.90 cm and 100 cm) (below) using the Principal Component, Multiplicative and Brovery methods (from left to right correspondingly).

aerial and satellite imagery. It was only the very vague, deep and smaller sized features (e.g. posthole/palisade traces) that were not able to be discriminated via the various remote sensing platforms. Still, the fusion of the above data may hinder a potential value for a more systematic study.

The experimental employment of ground hyperspectral data, as a mean of experimental remote sensing approach, was successful since the resulting maps have been verified both from satellite imagery and ground geophysical surveys. Although the area investigated covered only part of the tell, useful conclusions may arise from the fusion of all these techniques. A further detailed observation of the results shows that geophysical anomalies found at depths more than 1.3 m below the surface are not detectable from ground spectroradiometric data. Furthermore, several indices applied in this archaeological investigation showed that a number of non-conventional indices may be of value for archaeological prospection.

Acknowledgements

Ground hyperspectral measurements results are part of the PhD thesis of Mr. Athos Agapiou. The authors would like to express their appreciation to the Alexander Onassis Foundation for funding the PhD study. Also thanks are given to the Remote Sensing Laboratory of the Department of Civil Engineering & Geomatics at the Cyprus University of Technology for supporting the particular PhD research (http://www.cut.ac.cy). The fieldwork campaign was supported by USA-NSF (U.S.-Hungarian-Greek Collaborative International

Research Experience for Students on Origins and Development of Prehistoric European Villages), Wenner-Gren Foundation (International Collaborative Research Grant, "Early Village Social Dynamics: Prehistoric Settlement Nucleation On The Great Hungarian Plain") and the Culture 2007-2013 Programme of the European Union (Archaeolandscapes Europe project). We are indebted to all of them.

References

Agapiou, A., Hadjimitsis, D.G., 2011. Vegetation indices and field spectro-radiometric measurements for validation of buried architectural remains: verification under area surveyed with geophysical campaigns. Journal of Applied Remote Sensing 5, 053554–053561.

Agapiou, A., Hadjimitsis, G.D., Sarris, A., Themistocleous, K., Papadavid, G., 2010. Hyperspectral ground truth data for the detection of buried architectural remains. Lecture Notes of Computer Science 6436, 318–331.

Agapiou, A., Hadjimitsis, D.G., Alexakis, D., Sarris, A., 2012. Observatory validation of Neolithic tells ("Magoules") in the Thessalian plain, central Greece, using hyperspectral spectroradiometric data. Journal of Archaeological Science. http://dx.doi.org/10.1016/j.jas.2012.01.001.

Alexakis, D., Sarris, A., 2010. Environmental and human risk assessment of the prehistoric and historic archaeological sites of Western Crete (Greece) with the use of GIS, remote sensing, fuzzy logic and neural networks. In: Ioannides, Marinos, Fellner, Dieter, Georgopoulos, Andreas, Hadjimitsis, Diofantos G. (Eds.), Lecture Notes in Computer Science No. 6436: Digital Heritage (Third International Conference, EuroMed 2010, Lemessos, Cyprus, November 8–13, 2010 Proceedings) – Remote Sensing for Archaeology and Cultural Heritage Management and Monitoring. Springer, pp. 332–342.

Alexakis, D., Sarris, A., Astaras, T., Albanakis, K., 2009. Detection of Neolithic settlements in Thessaly (Greece) through multispectral and hyperspectral satellite imagery. Sensors 9, 1167–1187.

Alexakis, A., Sarris, A., Astaras, T., Albanakis, K., 2011. Integrated GIS, remote sensing and geomorphologic approaches for the reconstruction of the landscape habitation of Thessaly during the Neolithic period. Journal of Archaeological Science 38, 89–100.

Altaweel, M., 2005. The use of ASTER satellite imagery in archaeological contexts. Archaeological Prospection 12, 151–166.

Aqdus, A.S., Hanson, S.W., Drummond, J., 2012. The potential of hyperspectral and multi-spectral imagery to enhance archaeological cropmark detection: a comparative study. Journal of Archaeological Science 39 (7), 1915–1924. http://dx.doi.org/10.1016/j.jas.2012.01.034.

Baret, F., Guyot, G., 1991. Potentials and limits of vegetation indices for LAI and APAR assessment. Remote Sensing of Environment 35 (2–3), 161–173.

Batayneh, T.A., 2011. Archaeogeophysics–archaeological prospection – a mini review. Journal of King Saud University – Science 23 (1), 83–89. http://dx.doi.org/10.1016/j.jksus.2010.06.011.

Cardarelli, E., Filippo, Di G., 2009. Integrated geophysical methods for the characterisation of an archaeological site (Massenzio Basilica — Roman forum, Rome, Italy). Journal of Applied Geophysics 68 (4), 508–521. http://dx.doi.org/10.1016/j.jappgeo.2009.02.009.

Castro-Esau, K.L., Sánchez-Azofeifa, G.A., Rivard, B., 2006. Comparison of spectral indices obtained using multiple spectroradiometers. Remote Sensing of Environment 103, 276–288.

Cavalli, R.S., Colosi, F., Palombo, A., Pignatti, S., Poscolieri, M., 2007. Remote hyperspectral imagery as a support to archaeological prospection. Journal of Cultural Heritage 8, 272–283.

Chase, F.A., Chase, Z.D., Weishampel, F.J., Drake, B.J., Shrestha, L.R., Slatton, C.K., Awe, J.J., Carter, E.W., 2011. Airborne LiDAR, archaeology, and the ancient Maya landscape at Caracol, Belize. Journal of Archaeological Science 38 (2), 387–398. http://dx.doi.org/10.1016/j.jas.2010.09.018.

De Laet, V., Paulissen, E., Waelkens, M., 2007. Methods for the extraction of archaeological features from very high-resolution Ikonos-2 remote sensing imagery, Hisar (southwest Turkey). Journal of Archaeological Science 34 (5), 830–841.

Drahor, G.M., 2011. A review of integrated geophysical investigations from archaeological and cultural sites under encroaching urbanisation in İzmir, Turkey. Physics and Chemistry of the Earth 36 (16), 1294–1309. http://dx.doi.org/10.1016/j.pce.2011.03.010.

Ernenwein, G.E., 2009. Integration of multidimensional archaeogeophysical data using supervised and unsupervised classification. Near Surface Geophysics, 147–158.

Gitelson, A., Merzlyak, M.N., 1994. Quantitative estimation of chlorophyll-a using reflectance spectra: experiments with autumn chestnut and maple leaves. Journal of Photochemistry and Photobiology B: Biology 22, 247–252.

Gitelson, A.A., Kaufman, Y.J., Merzlyak, M.N., 1996. Use of a green channel in remote sensing of global vegetation from EOS-MODIS. Remote Sensing of Environment 58 (3), 289–298.

Gitelson, A.A., Merzlyak, M.N., Chivkunova, O.B., 2001. Optical properties and nondestructive estimation of anthocyanin content in plant leaves. Photochemistry and Photobiology 74, 38–45.

Hadjimitsis, D.G., Themistocleous, K., Agapiou, A., Clayton, C.R.I., 2009. Multi-temporal study of archaeological sites in Cyprus using atmospheric corrected satellite remotely sensed data. International Journal of Architectural Computing 7 (1), 121–138. http://dx.doi.org/10.1260/147807709788549376.

Hadjimitsis, D.G., Agapiou, A., Alexakis, D., Sarris, A., 2011. Exploring natural and anthropogenic hazard risk for cultural heritage in Cyprus using remote sensing and GIS. International Journal of Digital Earth. http://dx.doi.org/10.1080/17538947.2011.602119.

Hegedűs, K., Makkay, J., 1987. Vésztő-Mágor: a Settlement of the Tisza Culture. In: Tálas, L., Raczky, P. (Eds.), The Late Neolithic of the Tisza Region: a Survey of Recent Excavations and Their Findings. Szolnok County Museums, Budapest-Szolnok, pp. 85–104.

Hegedűs, K., 1982. Vésztő-Mágori-domb. In: Ecsedy, I., Kovács, L., Maráz, B., Torma, I. (Eds.), Magyarország Régészeti Topográfiája VI. Békés Megye Régészeti Topográfiája: a Szeghalmi Járás (IV/1). Akadémiai Kiadó, Budapest, pp. 184–185.

Huete, A.R., Liu, H.Q., Batchily, K., van Leeuwen, W., 1997. A comparison of vegetation indices over a global set of TM images for EOS-MODIS. Remote Sensing of Environment 59, 440–451.

Jahjah, M., Ulivieri, C., Invernizzi, A., Parapetti, R., 2007. Archaeological remote sensing application pre-post war situation of Babylon archaeological site-Iraq. Acta Astronautica 61 (1–6), 121–130. http://dx.doi.org/10.1016/j.actaastro.2007.01.034.

Jeng, Y., Lee, L.-Y., Chen, C.-Y., Lin, M.-J., 2003. Integrated signal enhancements in magnetic investigation in archaeology. Journal of Applied Geophysics 53 (1), 31–48. http://dx.doi.org/10.1016/S0926-9851(03)00015-6.

Jordan, C.F., 1969. Derivation of leaf area index from quality of light on the forest floor. Ecology 50, 663–666.

Juhász, I., 2000. A Csolt nemzetség monostora. In: Kollár, T. (Ed.), A középkori Dél-Alföld és Szer. Szeged, pp. 281–304.

Kaufman, Y.J., Tanré, D., 1992. Atmospherically resistant vegetation index (ARVI) for EOS-MODIS. IEEE Transactions on Geoscience and Remote Sensing 30, 261–270.

Kim, M.S., Daughtry, C.S.T., Chappelle, E.W., McMurtrey III, J.E., Walthall, C.L., 1994. The Use of High Spectral Resolution Bands for Estimating Absorbed Photosynthetically Active Radiation (APAR). 6th Symposium on Physical Measurements and Signatures in Remote Sensing. Val D'Isere, France.

Kincey, M., Challis, K., 2010. Monitoring fragile upland landscapes: the application of airborne lidar. Journal for Nature Conservation 18 (2), 126–134.

Kvamme, K.L., 2006. Integrating multidimensional geophysical data. Archaeological Prospection 13, 57–72.

Lasaponara, R., Masini, N., 2011. Satellite remote sensing in archaeology: past, present and future perspectives. Journal of Archaeological Science 38 (9), 1995–2002. http://dx.doi.org/10.1016/j.jas.2011.02.002.

Makkay, J., 2004. Vésztő–Mágor. Ásatás a szülőföldön. Békés Megyei Múzeumok Igazgatósága, Békéscsaba.

Masini, N., Lasaponara, R., 2007. Investigating the spectral capability of QuickBird data to detect archaeological remains buried under vegetated and not vegetated areas. Journal of Cultural Heritage 8, 53–60.

Papadopoulos, N., Sarris, A., 2011. Integrated geophysical survey to characterize the subsurface properties below and around the area of Saint Andreas church (Loutraki, Greece). In: Proceedings of the 14th International Congress "Cultural Heritage and New Technologies", ISBN 978-3-200-02112-9, pp. 643–652.

Papadopoulos, G.N., Yi, J.-M., Kim, J.-H., Tsourlos, P., Tsokas, N.G., 2010. Geophysical investigation of tumuli by means of surface 3D electrical resistivity tomography. Journal of Applied Geophysics 70 (3), 192–205. http://dx.doi.org/10.1016/j.jappgeo.2009.12.001.

Pappu, S., Akhilesh, K., Ravindranath, S., Raj, U., 2010. Applications of satellite remote sensing for research and heritage management in Indian prehistory. Journal of Archaeological Science 37 (9), 2316–2331. http://dx.doi.org/10.1016/j.jas.2010.04.005.

Parcak, S.H., 2009. Satellite Remote Sensing for Archaeology. Routledge Taylor and Francis Group Press, London and New York.

Parkinson, W.A., 2006. Tribal boundaries: stylistic variability and social boundary maintenance during the transition to the Copper Age on the Great Hungarian Plain. Journal of Anthropological Archaeology 25, 33–58.

Peddle, D.R., White, H.P., Soffer, R.J., Miller, J.R., LeDrew, E.F., 2001. Reflectance processing of remote sensing spectroradiometer data. Computers, Geosciences 27, 203–213.

Peñuelas, J., Filella, I., Biel, C., Serrano, L., Savé, R., 1993. The reflectance at the 950–970 Nm region as an indicator of plant water status. International Journal of Remote Sensing 14, 1887–1905.

Peñuelas, J., Gamon, J.A., Fredeen, A.L., Merino, J., Field, C.B., 1994. Reflectance indices associated with physiological changes in nitrogen- and water-limited sunflower leaves. Remote Sensing of Environment 48, 135–146.

Pinty, B., Verstraete, M.M., 1992. GEMI: a non-linear index to monitor global vegetation from satellites. Plant Ecology 101 (1), 15–20.

Qi, J., Chehbouni, A., Huete, A.R., Kerr, Y.H., Sorooshian, S., 1994. A modified soil adjusted vegetation index. Remote Sensing of Environment 48 (2), 119–126.

Richardson, A.J., Wiegand, C.L., 1977. Distinguishing vegetation from soil background information. Photogrammetric Engineering and Remote Sensing 43, 15–41.

Roujean, J.L., Breon, F.M., 1995. Estimating PAR absorbed by vegetation from bidirectional reflectance measurements. Remote Sensing of Environment 51 (3), 375–384.

Rouse, J.W., Haas, R.H., Schell, J.A., Deering, D.W., Harlan, J.C, 1974. Monitoring the Vernal Advancements and Retrogradation (Green Wave Effect) of Nature Vegetation. NASA/GSFC Final Report, Greenbelt.

Rowlands, A., Sarris, A., 2007. Detection of exposed and subsurface archaeological remains using multi-sensor remote sensing. Journal of Archaeological Science 34, 795–803.

Sarris, A., Papadopoulos, N, 2011. Geophysical Investigations at Szeghalom – Kovácshalom, Vésztő-Mágor, Visztu, Hungary (KRAP 2010). Unpublished Technical Report, Laboratory of Geophysical-Satellite Remote Sensing, Archaeo-environment, Institute for Mediterranean Studies – Foundation of Research, Technology (F.O.R.T.H.), Rethymno, Crete, August 8, 2011.

Sarris, A., 2006. Geophysical Prospection Survey at Vésztő-Mágor (Vésztő 15) and Okány 16–Futás, Visztu, Hungary (2006). Unpublished Technical Report, Laboratory of Geophysical-Satellite Remote Sensing, Archaeo-environment, Institute for Mediterranean Studies – Foundation of Research, Technology (F.O.R.T.H.), Rethymno, Crete, September 10, 2006.

Sarris, A., 2008. Remote sensing approaches, geophysical. In: Pearsall, Deborah M. (Ed.), Encyclopedia of Archaeology. Academic Press, New York, pp. 1912–1921. http://dx.doi.org/10.1016/B978-012373962-9.00270-3.

Sarris, A., 2012. Multi+ or Manifold Geophysical Prospection? Computer Applications and Quantitative Methods in Archaeology (CAA 2012). Southampton, Great Britain.

Sims, D.A., Gamon, J.A., 2002. Relationships between leaf pigment content and spectral reflectance across a wide range of species, leaf structures and developmental stages. Remote Sensing of Environment 81, 337–354.

Słowik, M., 2012. Influence of measurement conditions on depth range and resolution of GPR images: the example of lowland valley alluvial fill (the Obra River, Poland). Journal of Applied Geophysics 85, 1–14.

Soldovieri, F., Bavusi, M., Giocoli, A., Piscitelli, S., Crocco, L., Vallianatos, F., Soupios, P., Sarris, A., 2008. A Comparison Between Two GPR Data Processing Techniques for Fracture Detection and Characterization. 70th EAGE Conference, Exhibition Incorporating SPE EUROPEC 2008, Rome, 2–12 June 2008.

Stagakis, S., Markos, N., Sykioti, O., Kyparissis, A., 2010. Monitoring canopy biophysical and biochemical parameters in ecosystem scale using satellite hyperspectral imagery: an application on a Phlomis fruticosa Mediterranean ecosystem using multiangular CHRIS/PROBA observations. Remote Sensing of Environment 114, 977–994.

Traviglia, A., Cottica, D., 2011. Remote sensing applications and archaeological research in the Northern Lagoon of Venice: the case of the lost settlement of Constanciacus. Journal of Archaeological Science 38 (9), 2040–2050. http://dx.doi.org/10.1016/j.jas.2010.10.024.

Traviglia, A., 2005. Integration of MIVIS Hyperspectral remotely sensed data and Geographical Information Systems to study ancient landscape: the Aquileia case study. An International Journal of Landscape Archaeology 2, 139–170.

Tucker, C.J., 1979. Red and photographic infrared linear combinations for monitoring vegetation. Remote Sensing of Environment 8 (2), 127–150.

Vogelmann, J.E., Rock, B.N., Moss, D.M., 1993. Red edge spectral measurements from sugar maple leaves. International Journal of Remote Sensing 14, 1563–1575.

Weston, D.G., 2001. Alluvium and geophysical prospection. Archaeological Prospection 8, 265–272. http://dx.doi.org/10.1002/arp.160.

Zarco-Tejada, P.J., Pushnik, J.C., Dobrowski, S., Ustin, S.L., 2003. Steady-state chlorophyll a fluorescence detection from canopy derivative reflectance and double-peak red-edge effects. Remote Sensing of Environment 84, 283–294.

Zarco-Tejada, P.J., Berjón, A., López-Lozano, R., Miller, J.R., Martín, P., Cachorro, V., González, M.R., de Frutos, A., 2005. Assessing vineyard condition with hyperspectral indices: leaf and canopy reflectance simulation in a row-structured discontinuous canopy. Remote Sensing of Environment 99, 271–287.